Dimensional reduction in $Cs_2AgBiBr_6$ enables long-term stable Perovskite-based gas sensing

Wen Ye[1,2], Hong-Zhen Lin [3], Menglong Li[1], Lihua Jiang[1], Dongyun Chen [1]✉ & Jian-Mei Lu [1]✉

Halide perovskite gas sensors have a low gas detection limit at room temperature, surpassing the performance of traditional metal oxide chemiresistors. However, they are prone to structural decomposition and performance loss due to the lack of coordination unsaturated surface metal ions and sensitivity to environmental factors such as water, oxygen, heat, and light. To address this issue, we present a general strategy: replacing the cation Cs^+ in inorganic perovskite $Cs_2AgBiBr_6$ with long-chain alkylamines. This modification synthesizes perovskite sensor materials that effectively block moisture and exhibit excellent stability under real-working conditions. The chemiresistors show high sensitivity and stability to CO gas, with $(BA)_4AgBiBr_8$ detecting CO at a limit of 20 ppb, maintaining performance after 270 days of continuous exposure to ambient air. The exceptional performance of $(BA)_4AgBiBr_8$ is elucidated through density functional theory calculations combined with sum frequency generation spectroscopy, marking a significant breakthrough in halide perovskite-based gas sensing by surpassing the stability and sensitivity of traditional sensors.

Gas sensing technology, which converts gas components into light and electrical signals, holds promise in environmental monitoring, safety alert systems, and disease diagnosis, offering significant potential in enhancing human safety and quality of life[1–3]. Despite their high sensitivity, low cost, and fast response times, metal oxide semiconductor gas sensors face challenges in miniaturization and performance due to high energy consumption and detection limits[4,5]. Halide perovskites, with their numerous active sites, high mobility, long diffusion lengths, and excellent tunability, are ideal for preparing high-performance chemical resistive gas sensors, offering significant improvements over traditional materials like metal oxides in detecting low-concentration gases[6–8]. Moreover, lead-free halide perovskites stand out for their environmentally friendly characteristics compared to traditional lead-

based counterparts. By eliminating lead, these materials significantly mitigate health and environmental risks, making them a sustainable choice for advanced sensor applications.

Halide perovskites are widely recognized to have intrinsic defect tolerance; however, moderate temperature, humidity, and sunlight can degrade bonds and lead to perovskite crystal decomposition[9–11]. Unsurprisingly, early perovskite gas sensors could only operate in air for a few days[12,13]. Since then, significant progress has been made, with some sensors demonstrating operational stability for 180 days exposure to the atmosphere and negligible loss of sensing performance[14]. Despite these improvements, current perovskite gas sensors still do not fully meet the requirements for gas sensing applications. Lead-free halide perovskites, by addressing the toxicity concerns associated with

[1]State Key Laboratory of Bioinspired Interfacial Materials Science, College of Chemistry Chemical Engineering and Materials Science, Collaborative Innovation Center of Suzhou Nano Science and Technology, National United Engineering Laboratory of Functionalized Environmental Adsorption Materials, Soochow University, Suzhou, China. [2]Key Laboratory of Intelligent Optoelectronic Devices and Chips of Jiangsu Higher Education Institutions, School of Physical Science and Technology, Suzhou University of Science and Technology, Suzhou 215009, China. [3]Department i-LAB, Suzhou Institute of Nano-Tech and Nano-Bionics (SINANO), Chinese Academy of Sciences, Suzhou, China. ✉e-mail: dychen@suda.edu.cn; lujm@suda.edu.cn

traditional perovskites, offer broader applicability, particularly in environments where environmentally responsible solutions are essential.

In this study, we prepared three lead-free two-dimensional hybrid double perovskites (2D HDPs) with varying cation sizes, all of which demonstrated remarkable environmental stability, remaining operational even after >270 days of exposure to the atmosphere. The characteristic feature of 2D HDPs is a large hydrophobic layer sandwiched between the perovskite inorganic layers, which effectively prevents water molecules from attacking the perovskite, thereby enhancing its environmental stability (Fig. 1). However, this structural improvement reduces the interaction between gas molecules and the perovskite surface. Notably, $(BA)_4AgBiBr_8$ ($BA = CH_3(CH_2)_3NH_3^+$) can effectively detect 20 ppb CO while maintaining stability, marking a breakthrough in the detection of ultra-low concentration CO. This finding highlights the potential of 2D HDPs to overcome the limitations of traditional halide perovskites in gas sensor technology, paving the way for the practical application of halide perovskite-based gas sensors.

Results

Preparation and structural characterization of the two-dimensional hybrid double perovskite sensors

The 3D $A_2B^IB^{III}X_6$ (X = halogen) double perovskite lattice consists of corner-sharing octahedrons, with small ions (Cs^+ and MA^+) occupying the cuboctahedral cavities at the A-site[15,16]. However, if larger organic cations replace the ions at the A-site, the 3D structure is transformed into a 2D HDP lattice of $A_4B^IB^{III}X_8$. This lattice comprises single sheets of corner-sharing $B-X$ octahedra, which are templated by ordered arrays of organic cations[17,18]. To enhance the environmental stability of halide double perovskites, we employed structural modifications by reducing the dimensions of double perovskites. Specifically, we synthesized three 2D HDPs, namely $(BA)_4AgBiBr_8$ ($BA = CH_3(CH_2)_3NH_3^+$), $(HA)_4AgBiBr_8$ ($HA = CH_3(CH_2)_5NH_3^+$), and $(OA)_4AgBiBr_8$ ($OA = CH_3(CH_2)_7NH_3^+$), by utilizing cations of different sizes (Fig. 2a).

First, BA/HA/OA, AgBr, and $BiBr_3$ were dissolved in a heated hydrobromic acid solution using the proper stoichiometry. The solution was then slowly cooled to facilitate the formation of $(BA)_4AgBiBr_8$, $(HA)_4AgBiBr_8$, and $(OA)_4AgBiBr_8$ crystals. Their morphologies, crystal phases, and elemental compositions were characterized by scanning electron microscopy (SEM) and transmission electron microscopy (TEM). SEM imaging showed that the three 2D HDPs exhibited flake-shaped structures with smooth surfaces and uniform thickness (Fig. 2b–d). High-resolution TEM (HRTEM) analysis revealed an interplane spacing of 3.2 Å in two vertical directions for $(BA)_4AgBiBr_8$, corresponding to the (200) plane of $(BA)_4AgBiBr_8$ (Supplementary Fig. 7). The presence of clear diffraction spots in the electron diffraction pattern further confirmed the high crystallinity of the three perovskites (Fig. 2e–g). Furthermore, energy-dispersive X-ray spectroscopy demonstrated the uniform distribution of Ag, Bi, and Br elements within the perovskite structures (Supplementary Figs. 8–10).

Next, we synthesized three different perovskite powders using a rapid cooling method and conducted a comprehensive analysis of their structure, thermal properties, and optical properties. To verify the phase and purity of the powder samples, we performed powder X-ray diffraction (PXRD) measurements. For the layered compounds, we observed the first prominent 2θ peaks corresponding to (001) at 6.5°, 5.0°, and 4.3° for $(BA)_4AgBiBr_8$, $(HA)_4AgBiBr_8$ and $(OA)_4AgBiBr_8$, respectively. This shift in the position of the (001) diffraction peak toward smaller angles is attributed to the increase in spacing between octahedral sheets as the length of the carbon chain increases. The materials were further characterized by attenuated total reflection Fourier transform infrared (ATR-FTIR) spectroscopy and Raman spectroscopy. ATR-FTIR analysis revealed changes in the characteristic peaks of $(BA)_4AgBiBr_8$ compared with pure n-butylamine. The N-H δ peak shifted from 1571–1575 cm^{-1}, and the CH_2 δ peak shifted from 1463–1472 cm^{-1}, indicating a clear interaction between the butylamine ligands within the perovskite and the metal halide (Fig. 2l). Similar shifts in characteristic peaks were observed for $(HA)_4AgBiBr_8$ and
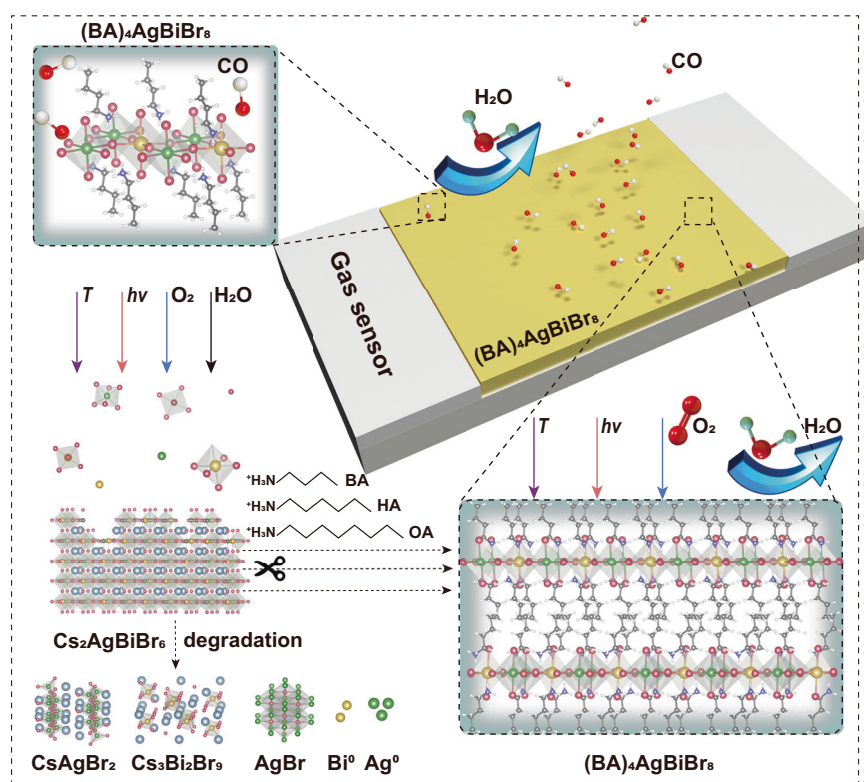
Fig. 1 | Schematic diagram of dimensional reduction in alkylamine-assisted 3D double perovskite to achieve long-term stable perovskite-based CO sensing. The black, white, purple, blue, yellow, green, and pink balls represent C, H, N, Cs, Bi, Ag, and Br atoms, respectively. T denotes temperature and hv represents incident light.
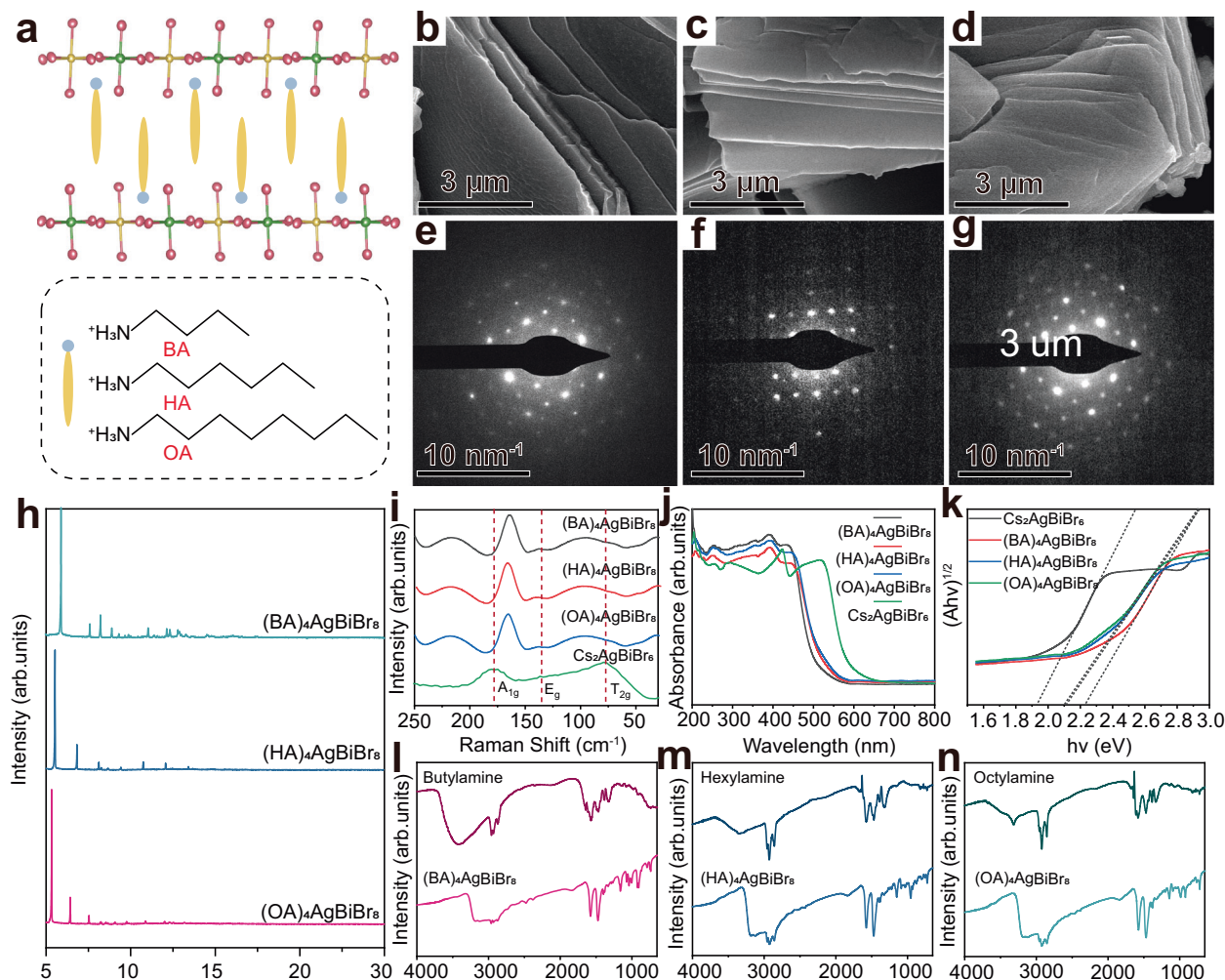
Fig. 2 | Structure and characterization of two-dimensional hybrid perovskites (2D HDPs). a Schematic diagram of the 2D HDPs structure. The yellow, green, and pink balls refer to Bi, Ag, and Br atoms, respectively. **b**–**d** Representative scanning electron microscopy (SEM) images of $(BA)_4AgBiBr_8$, $(HA)_4AgBiBr_8$, and $(OA)_4AgBiBr_8$ from three independently prepared samples ($n = 3$), showing similar morphological features. **e**–**g** High-resolution transmission electron microscopy (HRTEM) diffraction patterns of the corresponding samples. **h** Powder X-ray diffraction (PXRD) spectra. **i** Raman shift spectra. **j** Ultraviolet–visible (UV–vis) absorption spectra. **k** Tauc plot of $(Ah\nu)^{1/2}$ versus photon energy ($h\nu$) for $Cs_2AgBiBr_6$ and $(BA/HA/OA)_4AgBiBr_8$ Here, A is the absorption coefficient and $h\nu$ is the photon energy in eV. The linear region was extrapolated to estimate the optical band gap. **l**–**n** Attenuated total reflection Fourier transform infrared (ATR-FTIR) spectra of $(BA)_4AgBiBr_8$, $(HA)_4AgBiBr_8$, and $(OA)_4AgBiBr_8$. Source data are provided as a Source Data file.

$(OA)_4AgBiBr_8$ (Fig. 2m, n). Raman spectroscopy results for $Cs_2AgBiBr_6$ exhibited three well-defined peaks at 177.9, 135.2, and 77.4 cm^{-1}, corresponding to the A_{1g}, E_g, and T_{2g} vibrational modes, respectively (Fig. 2i)[19]. When introducing the organic layer, the A_{1g} peak associated with the stretching of $[AgBr_6]^{5-}$ and $[BiBr_6]^{3-}$ octahedra shifted to lower energy, the E_g peak shifted to higher energy, and the T_{2g} peak became weaker. These alterations are attributed to the distortion and separation of the octahedral sheets, leading to a softening of the phonon modes[19–21]. Thermogravimetric analysis results indicated that $Cs_2AgBiBr_6$ remained stable up to 410 °C, retaining over 99% of its initial weight (Supplementary Fig. 11). Two distinct weight loss steps were observed after exceeding 400 °C, with complete material decomposition occurring at 900 °C. The onset of thermal degradation for the 2D hybrid perovskite occurred around 200 °C, regardless of the length of the organic chain. The reduced thermal stability is attributed to the decomposition of the organic portion[19].

The optical properties were determined by examining the ultraviolet–visible absorption spectrum. $Cs_2AgBiBr_6$ demonstrated absorption around 600 nm, and the absorption peaks of all 2D hybrid perovskites were blue-shifted (Fig. 2j). The corresponding band gaps increased from 1.93 eV for $Cs_2AgBiBr_6$ to over 2.1 eV (Fig. 2k). This shift

in absorption and increase in band gap is ascribed to the differences in confinement effects and interactions between the constituent atoms of the crystal structures[22]. The introduction of organic cations increased the band gap by indirectly contributing to the asymmetry in the octahedral sheets, leading to intra- and inter-octahedral distortions. Such distortions are expected to affect the overlap of participating orbitals, consequently increasing the band gap[19].

To gain deeper insights into the structural changes occurring in the perovskite after dimensionality reduction, we employed density functional theory (DFT) calculations to simulate the crystal structure, energy band structure, and projected density of states (PDOS) for $Cs_2AgBiBr_6$ and $(BA)_4AgBiBr_8$, based on their crystallographic information files. The n-butylamine cation was used to transform the 3D parent structure of $Cs_2AgBiBr_6$ into a Ruddlesden−Popper-type layered perovskite, denoted as $(BA)_4AgBiBr_8$ (Fig. 3a, b). A noticeable difference was observed in the bond lengths between the two structures. In $Cs_2AgBiBr_6$, the Ag-Br bond length remains uniform at 2.80 Å throughout the 3D structure (Fig. 3c). However, in $(BA)_4AgBiBr_8$, significant bond length deviations were observed (Fig. 3d). The inorganic layer within $(BA)_4AgBiBr_8$ undergoes substantial distortion, particularly at the Ag site. In this structure, the Ag-Br octahedron undergoes
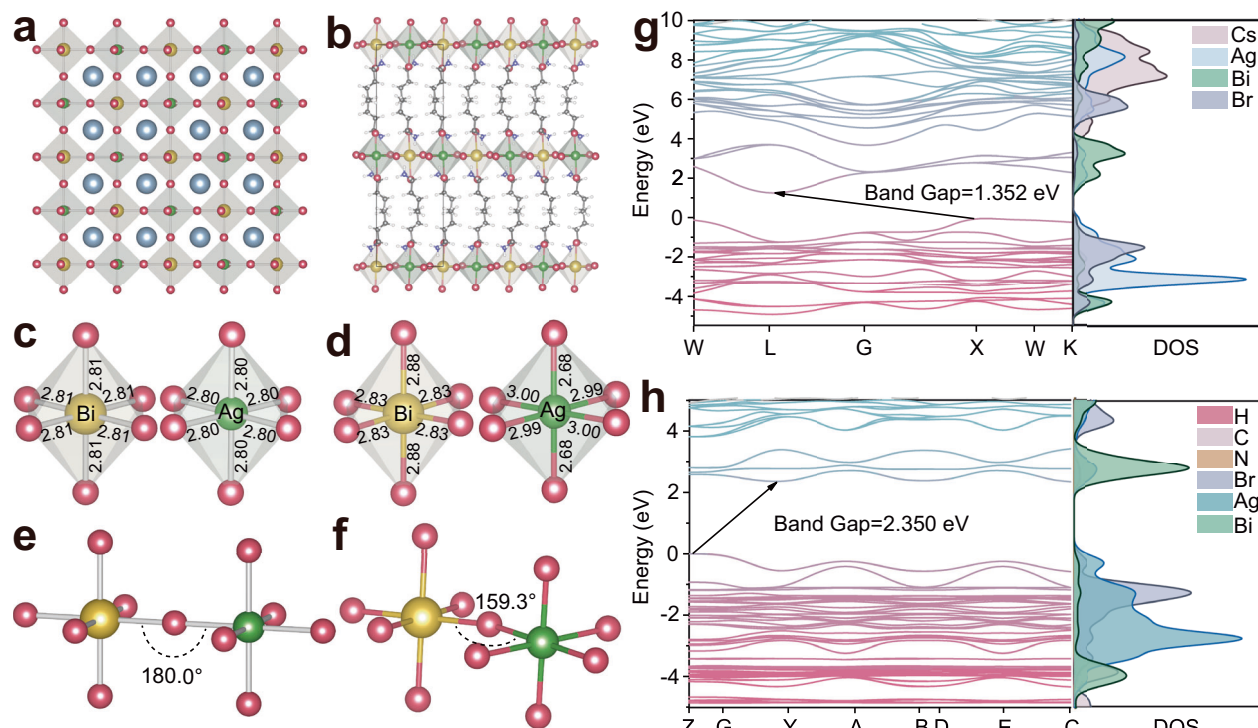
Fig. 3 | Crystal and energy band structure. Crystal structures of (**a**) $Cs_2AgBiBr_6$ and (**b**) $(BA)_4AgBiBr_8$. Ball and stick models showing the bond lengths (in Å) and in-plane connectivity of [$BiBr_6$] and [$AgBr_6$] octahedra for (**c**) $Cs_2AgBiBr_6$ and (**d**) $(BA)_4AgBiBr_8$. Bond angles of $M^I – X – M^{III}$ for (**e**) $Cs_2AgBiBr_6$ and (**f**) $(BA)_4AgBiBr_8$.

The black, white, purple, blue, yellow, green, and pink balls refer to C, H, N, Cs, Bi, Ag, and Br atoms, respectively. Calculated electronic band structure and atomic orbital projected density of states (PDOS) of (**g**) $Cs_2AgBiBr_6$ and (**h**) $(BA)_4AgBiBr_8$. Source data are provided as a Source Data file.

tetragonal distortion, with an unusually short bond length between Ag and the axial terminal bromine (Ag-Br_{ax} = 2.68 Å), whereas the bond length between Ag and the bridging equatorial bromides is longer (Ag-Br_{eq} = 3.00 Å; Fig. 3d). This distortion is primarily attributed to the mixing of filled transition metal nd orbitals with empty $(n + 1)s$ orbitals, which stabilizes the linear coordination geometry of Ag. In $Cs_2AgBiBr_6$, the Br-4p, Ag-4d, and Bi-6s orbitals contribute to the valence band maximum (VBM), and the conduction band minimum (CBM) is primarily generated by Bi-6p orbitals (Fig. 3g)[17,23–25]. In this case, the orbitals of the A-site cation do not contribute to the VBM or CBM. However, upon introducing organic cations, a significant increase in the band gap is observed (Fig. 3h), resulting from the distortion of octahedral structures and changes in the overlap of participating orbitals[19].

Gas sensing of the two-dimensional hybrid double perovskite-based sensors

Perovskites possess advantageous properties in various chemical applications owing to the active sites exposed by point defects and the ionic nature of the crystal lattice. To investigate this further, three 2D HDPs were employed as chemiresistive gas-sensing materials, and their performance was evaluated using carbon monoxide (CO) as the analyte. Figure 4a–c illustrate that the conductance of the three 2D hybrid perovskites increased rapidly upon exposure to CO and quickly recovered when air was reintroduced. A detailed comparison of response times, recovery times, and detection limits revealed that the incorporation of alkylamines significantly enhanced the performance of the $Cs_2AgBiBr_6$ sensor (Fig. 4d, Supplementary Figs. 12–17). Among the tested sensors, $(BA)_4AgBiBr_8$ exhibited the best overall performance, with a positive linear response to CO across concentrations ranging from 10 ppb to 400 ppb, achieving a detection limit as low as 20 ppb (Fig. 4d and Supplementary Fig. 17b). Using the root mean square deviation (RMSD) method[26,27], the theoretical detection limit of

the $(BA)_4AgBiBr_8$ sensor was calculated as 29.74 ppb, aligning closely with the experimental findings (See Supplementary Information for detailed calculation process). Additionally, $(HA)_4AgBiBr_8$ and $(OA)_4AgBiBr_8$ were tested under identical conditions. The $(HA)_4AgBiBr_8$ sensor achieved an experimental detection limit of 80 ppb and a theoretical detection limit of 103.59 ppb, while the $(OA)_4AgBiBr_8$ sensor exhibited an experimental detection limit of 120 ppb and a theoretical detection limit of 140.37 ppb (Supplementary Table 5). Real-time sensing curve cycling experiments for CO concentrations of 0.02, 0.2, 4, and 10 ppm were conducted to evaluate the stability and reproducibility of $(BA)_4AgBiBr_8$, $(HA)_4AgBiBr_8$, and $(OA)_4AgBiBr_8$ (Supplementary Figs. 18–20). All three sensors demonstrated similar initial response values across three consecutive assays, highlighting their stability and reproducibility. Importantly, replacing Cs^+ with alkyl chains significantly enhanced the environmental stability. The three perovskite-based sensors remained stable for over 270 days (Fig. 4f), marking a new record for perovskite-based sensors. As shown in Fig. 4g, this comparison is made using stability data compiled from previously published literature[12–14,28–59]. The complete list of sources is also provided in Supplementary Table 4. The low standard deviation in sensor responses further demonstrates the reliability of all three sensors (Supplementary Figs. 21–23).

To evaluate the effects of O_2 and H_2O concentrations on sensor performance, we adjusted the carrier gas composition and tested responses under varying oxygen (N_2, 20%, 60%, 100% O_2) and relative humidity (RH). The sensor's response decreased at 20% O_2 due to O_2 molecule occupation of exposed metal sites but improved at higher concentrations due to the formation of reactive oxygen species (Supplementary Figs. 24–26)[60]. Under low humidity, water adsorption hindered CO access to metal sites, reducing response, while high humidity enhanced the response of $(BA)_4AgBiBr_8$ (Supplementary Fig. 27), possibly due to material decomposition or denaturation, unlike $(HA)_4AgBiBr_8$ and $(OA)_4AgBiBr_8$ (Supplementary
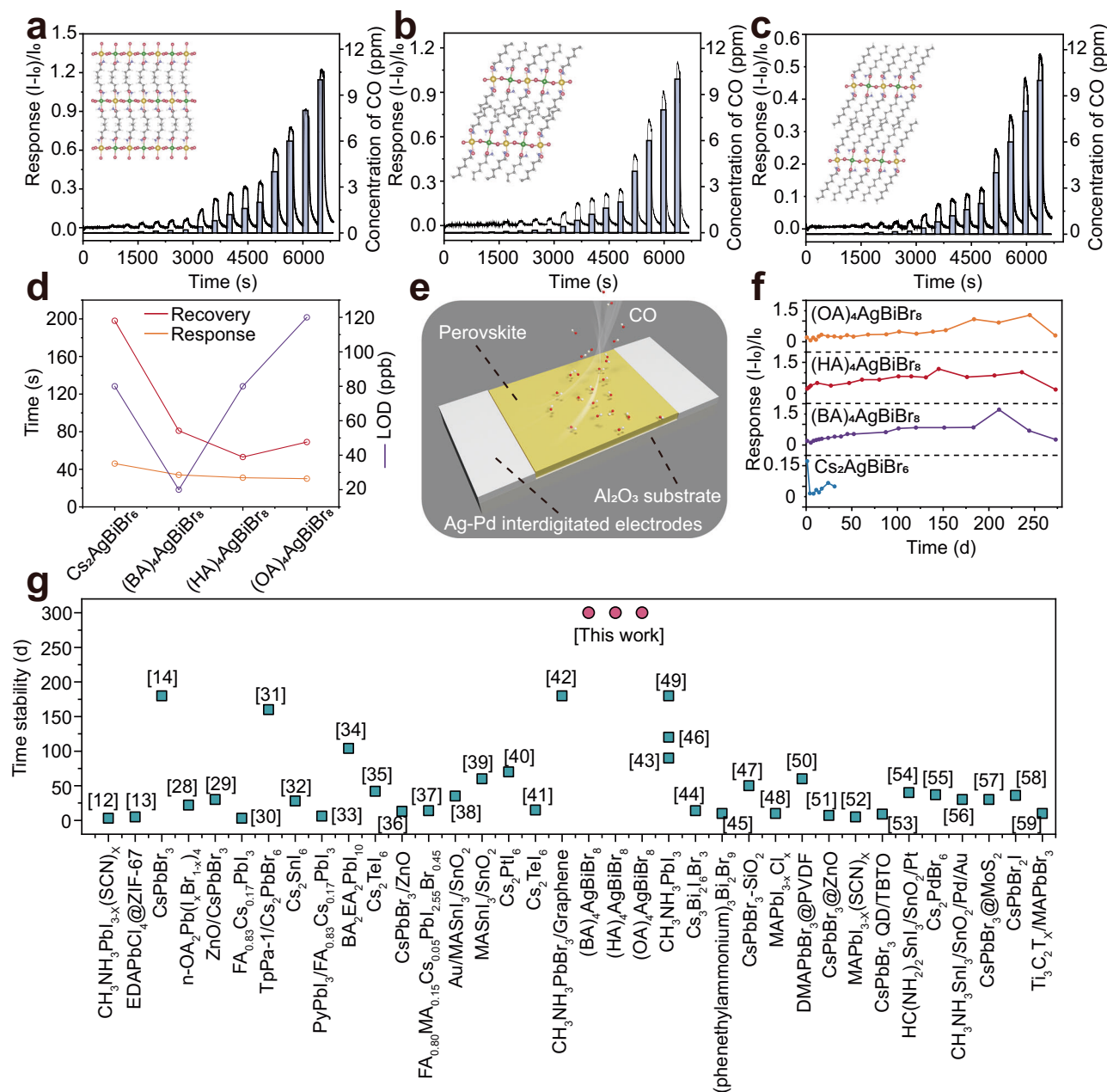
Fig. 4 | Sensing performance. Real-time response of (**a**) (BA)$_4$AgBiBr$_8$, (**b**) (HA)$_4$AgBiBr$_8$, and (**c**) (OA)$_4$AgBiBr$_8$ sensors with increasing concentrations of CO (from 10 ppb to 10 ppm). The insets show the corresponding perovskite crystal structures of each material. The black, white, purple, yellow, green, and pink balls refer to C, H, N, Bi, Ag, and Br atoms, respectively. **d** Comparison of response times, recovery times, and lower limits of detection (LOD) between Cs$_2$AgBiBr$_6$ and the three two-dimensional hybrid double perovskites (2D HDPs) is presented, with detailed measurements of response time, recovery time, and lower limit of detection provided in Supplementary Figs. 13–17. **e** Schematic diagram of the perovskite sensing structure. **f** Comparison of long-term sensing stability among the four perovskites. **g** Long-term time stability of CO sensors based on various perovskite materials. Reference numbers next to the data points correspond to sources listed in the main text reference list[12–14,28–59]. The compiled data are detailed in Supplementary Table 4, which uses a separate reference list. Source data are provided as a Source Data file.

Figs. 28 and 29), which were protected by longer alkyl chains. XRD analysis confirmed structural changes in (BA)$_4$AgBiBr$_8$ with atmospheric exposure (Supplementary Fig. 30), while no significant changes were observed for (HA)$_4$AgBiBr$_8$ and (OA)$_4$AgBiBr$_8$ (Supplementary Figs. 31 and 32).

Mechanistic inferences

The sensing response of perovskite can be attributed to its semiconductor properties and the interactions between CO molecules and exposed active sites. The ionic lattice of perovskite facilitates CO adsorption at point defects through acid-base interactions, resulting in electron extraction and transfer from CO to (BA)$_4$AgBiBr$_8$, which alters the material's resistivity (Fig. 5a). To identify the optimal adsorption sites for CO molecules, we calculated the system's energy following CO adsorption, with the optimal adsorption configuration depicted in Supplementary Fig. 33. Charge difference density maps reveal distinct charge redistributions between CO and adsorption sites on (BA)$_4$AgBiBr$_8$ (Fig. 5a), indicating specific interactions. When CO adsorbs at exposed Bi sites, formed due to the absence of Br ions, a thicker electron accumulation layer is generated, leading to changes in
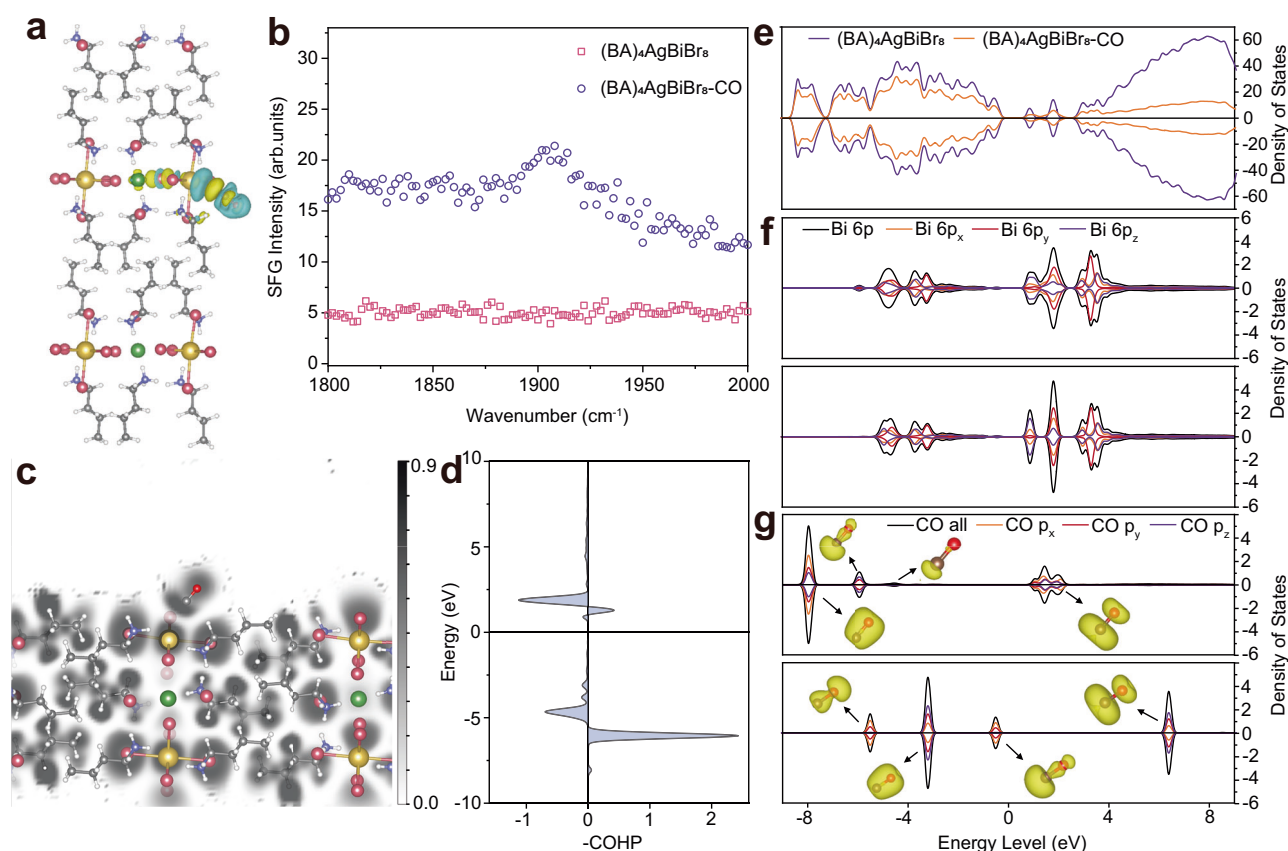
Fig. 5 | Characterization of the sensing mechanism. a The charge difference density of adsorption of CO on BA$_4$AgBiBr$_8$ (200) surface. The electron accumulation and depletion are represented with yellow and cyan contours, with isosurfaces being 0.003 e/Å^3. The black, white, purple, yellow, green, and pink balls refer to C, H, N, Bi, Ag, and Br atoms, respectively. Corresponding atomic coordinates are available in Supplementary Data 1. **b** Sum frequency generation (SFG) spectra of (BA)$_4$AgBiBr$_8$ film before and after CO adsorption. **c** The Electron Localization Function (ELF) diagram for adsorption of CO on BA$_4$AgBiBr$_8$ surface. The black, white, purple, yellow, green, and pink balls refer to C, H, N, Bi, Ag, and Br atoms, respectively. Corresponding atomic coordinates are available in Supplementary Data 2. **d** The Crystal Orbital Hamilton Population (COHP) and the corresponding Integrated Crystal Orbital Hamilton Population (ICOHP) value for C-Bi bond in the configuration of CO absorbed on BA$_4$AgBiBr$_8$ (200). The Fermi level (E$_f$) was set to 0.00 eV. **e** Total density of states (TDOS) of BA$_4$AgBiBr$_8$ (200) surface, and BA$_4$AgBiBr$_8$ (200) surface with CO molecule. The E$_f$ is set to 0.00 eV. **f** Projected density of states (PDOS) of 6p orbitals of Bi in the BA$_4$AgBiBr$_8$ (200) surface with a CO molecule absorbed and Bi in the clean BA$_4$AgBiBr$_8$ (200) surface. The E$_f$ is set to 0.00 eV. **g** PDOS of p orbitals of a CO molecule on the BA$_4$AgBiBr$_8$ (200) surface and an isolated CO molecule. The E$_f$ is set to 0.00 eV. The insets are the partial charge densities with isosurface level set to 0.02 e/Å. The electron accumulation is represented with yellow contour. Source data are provided as a Source Data file.

carrier concentration. This phenomenon was further confirmed by sum frequency generation (SFG) spectroscopy (Fig. 5b), where the SFG signal intensity of (BA)$_4$AgBiBr$_8$ increases significantly after CO treatment, suggesting charge transfer. Additionally, the presence of CO characteristic peaks in the SFG spectra indicates that CO molecules exhibit high orientation uniformity on the surface of (BA)$_4$AgBiBr$_8$ at room temperature.

To further clarify the interaction between CO and (BA)$_4$AgBiBr$_8$, we analyzed the density of states (DOS) before and after CO adsorption. Figure 5e shows negligible changes in the total density of states (TDOS) near the Fermi level of (BA)$_4$AgBiBr$_8$ after CO adsorption, suggesting weak orbital interactions. The projected density of states (PDOS) indicates that these weak interactions primarily originate from the p orbital of CO and the 6p orbital of Bi (Fig. 5f, g). Electron Localization Function (ELF) analysis further supports this conclusion, showing discontinuous electron distributions between CO and (BA)$_4$AgBiBr$_8$ (Fig. 5c), which is characteristic of physical adsorption. Additionally, Crystal Orbital Hamilton Population (COHP) analysis confirms weak orbital coupling (Fig. 5d), as evidenced by minimal antibonding characteristics (few positive COHP values) and a low Integrated Crystal Orbital Hamilton Population (ICOHP) value (-0.53 eV). Although these

results indicate that CO molecules undergo physical adsorption on the surface of (BA)$_4$AgBiBr$_8$, the observed significant charge transfer and excellent sensing performance may arise from the strong localized charge redistribution around adsorption sites, which facilitates rapid response and recovery (Fig. 4a).

Discussion

This study advances the field of gas sensing by addressing the limitations of halide perovskite sensors through innovative material modifications. By replacing the cation Cs$^+$ in Cs$_2$AgBiBr$_6$ with long-chain alkylamines, we have developed perovskite materials that effectively mitigate structural decomposition and performance degradation induced by environmental factors. The resultant sensor, (BA)$_4$AgBiBr$_8$, demonstrates exceptional performance with a CO detection limit of 20 ppb and maintains its stability after 270 days of continuous exposure to ambient air. The sensing performance was excellent compared to all other reported electric CO sensors as summarized in Supplementary Table 5. This achievement marks a significant improvement over perovskite sensors and highlights the effectiveness of using two-dimensional hybrid double perovskites to enhance sensor durability and sensitivity. This breakthrough paves the way for practical applications in environmental monitoring, safety systems, and disease

diagnosis, thereby significantly advancing the potential of halide perovskite-based gas sensing technology.

Methods

Synthesis of $(BA)_4AgBiBr_8$

In the synthesis of the product, 0.9 mmol of AgBr, 0.9 mmol of $BiBr_3$, and 3.6 mmol of n-butylamine solution were added to a 5 mL round bottom flask. Then, 2.6 mL of 48% HBr was added to the flask. The mixture was stirred at 100 °C until all the reactants were completely dissolved. The resulting solution was allowed to cool to room temperature naturally, and the product was obtained. Subsequently, the product was washed multiple times with diethyl ether and dried under vacuum at 60 °C for 10 h.

Synthesis of $(HA)_4AgBiBr_8$

In the synthesis of the product, 0.9 mmol of AgBr, 0.9 mmol of $BiBr_3$, and 3.6 mmol of n-hexylamine solution were added to a 5 mL round bottom flask. Then, 2.6 mL of 48% HBr was added to the flask. The mixture was stirred at 130 °C until all the reactants were completely dissolved. The resulting solution was allowed to cool to room temperature naturally, and the product was obtained. Subsequently, the product was washed multiple times with diethyl ether and dried under vacuum at 60 °C for 10 h.

Synthesis of $(OA)_4AgBiBr_8$

In the synthesis of the product, 0.9 mmol of AgBr, 0.9 mmol of $BiBr_3$, and 3.6 mmol of n-octylamine solution were added to a 5 mL round bottom flask. Then, 2.6 mL of 48% HBr was added to the flask. The mixture was stirred at 140 °C until all the reactants were completely dissolved. The resulting solution was allowed to cool to room temperature naturally, and the product was obtained. Subsequently, the product was washed multiple times with diethyl ether and dried under vacuum at 60 °C for 10 h.

Fabrication of the sensors

Ultrasonically disperse 20 mg of $(BA)_4AgBiBr_8$ in 1 mL of chlorobenzene. Then, apply 20 μL of the dispersion onto an Al_2O_3 substrate that has been printed with Ag-Pd interdigitated electrodes. The channel width of the electrodes is 200 μm (MJ-10, Beijing Elite Technology Co. Ltd, China). Subsequently, dry the coating for 5 min under an infrared drying lamp.

Gas sensing measurements

The performance of the $(BA)_4AgBiBr_8$ sensor was assessed by measuring the current under varying concentrations of CO/Air gas flow at 25 °C. A sealed chamber with gas input, gas exit, and electrical feed, having a capacity of 1200 cm^3, was utilized to power the sensor. To monitor the current, DC current-time (I-T) measurements were conducted using a Keithley 4200-SCS instrument. Each I-T measurement lasted for 4 min to ensure accurate and precise experimental data. Prior to introducing the target gas, the chamber was purged with dry air until the sensor's current stabilized. During the experiments, the airflow rate was maintained at 100 mL/min to minimize its influence on the measurements.

Material characterization and spectroscopic investigation

Scanning electron microscopy (SEM) and energy-dispersive X-ray spectroscopy (EDS) spectra were acquired using a HITACHI Regulus 8230 cold field emission SEM at an acceleration voltage of 15 kV. High-resolution transmission electron microscopy (HRTEM), and selected area electron diffraction (SAED) were performed on a Talos F200X G2 electron microscope (Thermo Scientific) at 200 kV. The structural properties of the perovskite were analyzed using X-ray diffraction (XRD) with a Bruker D8 Advance and Fourier-transform infrared

spectroscopy (FTIR) with an IRTracer-100. Sensor performance was evaluated using a Keithley 4200-SCS instrument. The sum frequency generation (SFG) spectrometer laser system was configured by EKSPLA.

Theoretical calculation

All of the structural relaxation and electronic structure calculations were performed using the density functional theory (DFT), as implemented in the Vienna Ab initio Simulation Package (VASP)[29,30,61,62]. The exchange-functional was treated within the generalized gradient approximation (GGA) of the Perdew-Burke-Ernzerhof (PBE) functional[63–65]. The core and valence electronic interactions were described using the frozen-core projector augmented-wave (PAW) potentials[66]. The $(BA)_4AgBiBr_8$ (200) surface model was constructed for theoretical calculations. The convergence criteria of the force and energy change were 0.01 eV $Å^{-1}$ and 1×10^{-4} eV per atom in the geometry optimization. The cut-off energy of the plane-wave basis was set as 400 eV to optimize the calculations for atoms and cell optimization. The k-point sampling was modeled from the Gamma scheme with a $3 \times 1 \times 1$ mesh. To avoid interactions between periodic slabs, lattice parameters in the direction perpendicular to the surface were set as 25 Å. The DFT-D3 method was used to evaluate the long-range van der Waals (vdW) contributions[67].

Reporting summary

Further information on research design is available in the Nature Portfolio Reporting Summary linked to this article.

Data availability

The data generated in this study are provided in the Supplementary Information and Source Data file. Source data are provided with this paper. The atomic coordinates of the DFT-optimized structures shown in Fig. 5a and c, and Supplementary Fig. 33 are provided as Supplementary Data 1–3 in plain-text format. Source data are provided with this paper.

References

1. Kaushik, A. et al. Organic-inorganic hybrid nanocomposite-based gas sensors for environmental monitoring. *Chem. Rev.* **115**, 4571–4606 (2015).
2. Modi, A., Koratkar, N., Lass, E., Wei, B. & Ajayan, P. M. Miniaturized gas ionization sensors using carbon nanotubes. *Nature* **424**, 171–174 (2003).
3. Turner, A. P. & Magan, N. Electronic noses and disease diagnostics. *Nat. Rev. Microbiol.* **2**, 161–166 (2004).
4. Dey, A. Semiconductor metal oxide gas sensors: a review. *J. Mater. Sci. Eng. B* **229**, 206–217 (2018).
5. Ji, H., Zeng, W. & Li, Y. Gas sensing mechanisms of metal oxide semiconductors: a focus review. *Nanoscale* **11**, 22664–22684 (2019).
6. Jena, A. K., Kulkarni, A. & Miyasaka, T. Halide perovskite photovoltaics: background, status, and future prospects. *Chem. Rev.* **119**, 3036–3103 (2019).
7. Zhu, H. et al. Efficient and stable large bandgap $MAPbBr_3$ perovskite solar cell attaining an open circuit voltage of 1.65 V. *ACS Energy Lett.* **7**, 1112–1119 (2022).
8. Younis, A. et al. Halide perovskites: a new era of solution-processed electronics. *Adv. Mater.* **33**, 2005000 (2021).
9. Dualeh, A., Gao, P., Seok, S. I., Nazeeruddin, M. K. & Grätzel, M. Thermal behavior of methylammonium lead-trihalide perovskite photovoltaic light harvesters. *Chem. Mater.* **26**, 6160–6164 (2014).
10. Kim, G. Y. et al. Large tunable photoeffect on ion conduction in halide perovskites and implications for photodecomposition. *Nat. Mater.* **17**, 445–449 (2018).

11. Tai, Q. et al. Efficient and stable perovskite solar cells prepared in ambient air irrespective of the humidity. *Nat. Commun.* **7**, 11105 (2016).

12. Zhuang, Y., Yuan, W., Qian, L., Chen, S. & Shi, G. High-performance gas sensors based on a thiocyanate ion-doped organometal halide perovskite. *Phys. Chem. Chem. Phys.* **19**, 12876–12881 (2017).

13. Lu, Z., Lou, C., Cheng, A., Zhang, J. & Sun, J. A sensitive and ultrafast $FA_{0.83}Cs_{0.17}PbI_3$ perovskite sensor for NO_2 detection at room temperature. *J. Alloy. Compd.* **919**, 165831 (2022).

14. Casanova-Cháfer, J., García-Aboal, R., Atienzar, P. & Llobet, E. Gas sensing properties of perovskite decorated graphene at room temperature. *Sensors* **19**, 4563 (2019).

15. Igbari, F., Wang, Z. K. & Liao, L. S. Progress of lead-free halide double perovskites. *Adv. Energy Mater.* **9**, 1803150 (2019).

16. Luo, J. et al. Efficient and stable emission of warm-white light from lead-free halide double perovskites. *Nature* **563**, 541–545 (2018).

17. Connor, B. A., Leppert, L., Smith, M. D., Neaton, J. B. & Karunadasa, H. I. Layered halide double perovskites: dimensional reduction of $Cs_2AgBiBr_6$. *J. Am. Chem. Soc.* **140**, 5235–5240 (2018).

18. Vargas, B., Rodríguez-López, G. N. & Solis-Ibarra, D. The emergence of halide layered double perovskites. *ACS Energy Lett.* **5**, 3591–3608 (2020).

19. Sikarwar, P., Siwach, P., Chandra, N. V. P., Antharjanam, S. & Chandiran, A. K. Dimensional reduction of $Cs_2AgBiBr_6$ using alkyl ammonium cations $CH_3(CH_2)_n NH_3^+$ (n = 1, 2, 3, and 6) of varying chain lengths and their role in structural and optoelectronic properties. *Inorg. Chem.* **62**, 5836–5844 (2023).

20. Schmitz, F. et al. Large cation engineering in two-dimensional silver-bismuth bromide double perovskites. *Chem. Mater.* **33**, 4688–4700 (2021).

21. Manna, D. et al. Lattice dynamics and electron-phonon coupling in lead-free $Cs_2AgIn_{1-x}Bi_xCl_6$ double perovskite nanocrystals. *J. Phys. Chem. Lett.* **11**, 2113–2120 (2020).

22. Mao, L. et al. Chemical and structural diversity of hybrid layered double perovskite halides. *J. Am. Chem. Soc.* **141**, 19099–19109 (2019).

23. Schmitz, F. et al. Lanthanide-induced photoluminescence in lead-free $Cs_2AgBiBr_6$ bulk perovskite: insights from optical and theoretical investigations. *J. Phys. Chem. Lett.* **11**, 8893–8900 (2020).

24. McClure, E. T., Ball, M. R., Windl, W. & Woodward, P. M. $Cs_2AgBiBr_6$ (X = Br, Cl): new visible light absorbing, lead-free halide perovskite semiconductors. *Chem. Mater.* **28**, 1348–1354 (2016).

25. Ji, F. et al. Lead-free halide double perovskite $Cs_2AgBiBr_6$ with decreased band gap. *Angew. Chem., Int. Ed.* **132**, 15303–15306 (2020).

26. Ammu, S. et al. Flexible, all-organic chemiresistor for detecting chemically aggressive vapors. *J. Am. Chem. Soc.* **134**, 4553–4556 (2012).

27. Li, J. et al. Carbon nanotube sensors for gas and organic vapor detection. *Nano Lett.* **3**, 929–933 (2003).

28. Zhu, S. et al. Novel cubic gravel-like $EDAPbCl_4$@ZIF-67 as electrochemical sensor for the detection of protocatechuic acid. *J. Alloy. Compd.* **903**, 163946 (2022).

29. Brintakis, K. et al. Ligand-free all-inorganic metal halide nanocubes for fast, ultra-sensitive and self-powered ozone sensors. *Nanoscale Adv.* **1**, 2699–2706 (2019).

30. John, A. T. et al. Mixed-dimensional organic-inorganic metal halide perovskite (OIMHP) based gas sensors with superior stability for NO_2 detection. *Mater. Adv.* **3**, 1263–1271 (2022).

31. Chizhov, A. et al. Photoresistive gas sensor based on nanocrystalline ZnO sensitized with colloidal perovskite $CsPbBr_3$ nanocrystals. *Sens. Actuators B Chem.* **329**, 129035 (2021).

32. Ye, W. et al. Halide perovskite glues activate two-dimensional covalent organic framework crystallites for selective NO_2 sensing. *Nat. Commun.* **14**, 2133 (2023).

33. Hung, P. T. et al. Growth and NO_2 sensing properties of Cs_2SnI_6 thin film. *Mater. Res. Bull.* **147**, 111628 (2022).

34. Cheng, A. et al. Hybrid 1D/3D-structured perovskite as a highly selective and stable sensor for NO_2 detection at room temperature. *Molecules* **28**, 2615 (2023).

35. Han, S., Wang, G.-E., Xu, G., Luo, J. & Sun, Z. Ferroelectric perovskite-type films with robust in-plane polarization toward efficient room-temperature chemiresistive sensing. *Fundam. Res.* **3**, 362–368 (2023).

36. Hoat, P. D. et al. Synthesis of Cs_2TeI_6 thin film and its NO_2 gas-sensing properties under blue-light illumination. *Scr. Mater.* **207**, 114305 (2022).

37. Li, Y. et al. $CsPbBr_3$ quantum dots enhanced ZnO sensing to NO_2 at room temperature. *Sens. Actuators B Chem.* **368**, 132189 (2022).

38. Chen, H. et al. Superior self-charged and -powered chemical sensing with high performance for NO_2 detection at room temperature. *Adv. Opt. Mater.* **8**, 1901863 (2020).

39. Chen, Y. et al. Light enhanced room-temperature resistive NO_2 sensor based on a gold-loaded organic-inorganic hybrid perovskite incorporating tin dioxide. *Microchim. Acta* **186**, 1–10 (2019).

40. Hien, V. X. et al. Room-temperature NO_2 sensor based on a hybrid nanomaterial of methylammonium tin iodide submicron spheres and tin dioxide nanowires. *Scr. Mater.* **188**, 107–111 (2020).

41. Chen, Z.-K. et al. Lead-free halide Cs_2PtI_6 perovskite favoring Pt–N bonding for trace NO detection. *ACS Sens* **6**, 3800–3807 (2021).

42. Chen, Z.-K. et al. Surface functionalization of ion-in-conjugation polymer sensors for humidity-independent gas detection at room temperature. *Sens. Actuators B Chem.* **372**, 132654 (2022).

43. Maity, A., Raychaudhuri, A. & Ghosh, B. High sensitivity NH_3 gas sensor with electrical readout made on paper with perovskite halide as sensor material. *Sci. Rep.* **9**, 7777 (2019).

44. Jiao, W., He, J. & Zhang, L. Fabrication and investigation of a new all-inorganic lead-free perovskite $Cs_3Bi_2I_6Br_3$ for ammonia detection at room temperature. *J. Alloy. Compd.* **895**, 162561 (2022).

45. Li, G. et al. Bismuth-based lead-free perovskite film for highly sensitive detection of ammonia gas. *Sens. Actuators B Chem.* **345**, 130298 (2021).

46. Maity, A. et al. Universal sensing of ammonia gas by family of lead halide perovskites based on paper sensors: experiment and molecular dynamics. *Mater. Res. Bull.* **136**, 111142 (2021).

47. Huangfu, C., Wang, Y., Wang, Z., Hu, Q. & Feng, L. A stable and humidity-resistant NH_3 sensor based on luminous $CsPbBr_3$ perovskite nanocrystals. *Talanta* **253**, 124070 (2023).

48. Sheikh, A. D., Vhanalakar, V., Katware, A., Pawar, K. & Kulkarni, S. Ultrasensitive organic-inorganic nanotube thin films of halogenated perovskites as room-temperature ammonia sensors. *J. Alloy. Compd.* **894**, 162388 (2022).

49. Maity, A. & Ghosh, B. Fast response paper-based visual color change gas sensor for efficient ammonia detection at room temperature. *Sci. Rep.* **8**, 16851 (2018).

50. Huang, G. et al. An effective and reliable fluorescent sensor for selective detection of methylamine gas based on in-situ formation of $MAPbBr_3$ perovskite nanocrystals in electrospun fibers. *Sens. Actuators B Chem.* **347**, 130618 (2021).

51. Xuan, W. et al. Machine learning-assisted sensor based on $CsPbBr_3$@ZnO nanocrystals for identifying methanol in mixed environments. *ACS Sens* **8**, 1252–1260 (2023).

52. Lee, K.-Y. et al. Ultrasensitive detection of hydrogen sulfide gas based on perovskite vertical channel chemo-sensor. *Sens. Actuators B Chem.* **326**, 128988 (2021).

53. Shan, H. et al. Room-temperature hydrogen sulfide sensor based on tributyltin oxide functionalized perovskite $CsPbBr_3$ quantum dots. *ACS Appl. Nano Mater.* **5**, 6801–6809 (2022).

54. Zhang, X. et al. Effects of organotin halide perovskite and Pt nanoparticles in SnO_2-based sensing materials on the detection of

formaldehyde. *J. Mater. Sci. Mater. Electron.* **30**, 20624–20637 (2019).

55. Ye, W. et al. Surfactant-free, one-step synthesis of lead-free perovskite hollow nanospheres for trace CO detection. *Adv. Mater.* **33**, 2100674 (2021).

56. Liu, H., Chen, Y., Dong, Z., Wang, X. & Xu, J. The preparation of $CH_3NH_3SnI_3/SnO_2/Pd/Au$ gas sensor material for detecting CO and the function of each component. *J. Mater. Sci. Mater. Electron.* **33**, 7463–7476 (2022).

57. Xu, X. et al. $CsPbBr_3$-based nanostructures for room-temperature sensing of volatile organic compounds. *ACS Appl. Mater. Interfaces* **14**, 39524–39534 (2022).

58. Chen, H. et al. Light-activated inorganic $CsPbBr_2I$ perovskite for room-temperature self-powered chemical sensing. *Phys. Chem. Chem. Phys.* **21**, 24187–24193 (2019).

59. Hu, J. et al. MXene/perovskite-based bionic human odor sensor array with machine learning. *Chem. Eng. J.* **468**, 143752 (2023).

60. Zhou, K. et al. Recent advances in structure design and application of metal halide perovskite-based gas sensor. *ACS Sens* **9**, 4425–4449 (2024).

61. Kresse, G. & Furthmüller, J. Efficient iterative schemes for ab initio total-energy calculations using a plane-wave basis set. *Phys. Rev. B* **54**, 11169 (1996).

62. Kresse, G. & Hafner, J. Ab initio molecular dynamics for open-shell transition metals. *Phys. Rev. B* **48**, 13115 (1993).

63. Perdew, J. P. & Wang, Y. Accurate and simple analytic representation of the electron-gas correlation energy. *Phys. Rev. B* **45**, 13244 (1992).

64. Perdew, J. P., Burke, K. & Wang, Y. Generalized gradient approximation for the exchange-correlation hole of a many-electron system. *Phys. Rev. B* **54**, 16533 (1996).

65. Perdew, J. P., Burke, K. & Ernzerhof, M. Generalized gradient approximation made simple. *Phys. Rev. Lett.* **77**, 3865 (1996).

66. Blöchl, P. E. Projector augmented-wave method. *Phys. Rev. B* **50**, 17953 (1994).

67. Grimme, S., Antony, J., Ehrlich, S. & Krieg, H. A consistent and accurate ab initio parametrization of density functional dispersion correction (DFT-D) for the 94 elements H–Pu. *J. Chem. Phys.* **132**, 154104 (2010).

Acknowledgements

Author contributions

J.-M.L. and D.Y.C. conceived and directed the project. W.Y. carried out key experiments and wrote the manuscript. H.-Z.L. performed sum-frequency generation testing and analysis. W.Y., M.L.L. and L.H.J. performed density functional theory calculations and conducted part of the characterizations. W.Y., M.L.L., L.H.J., D.Y.C. and J.-M.L. analysed the data. All authors discussed the results and commented on the manuscript.

Competing interests

The authors declare no competing interests.

Additional information

Supplementary information The online version contains supplementary material available at https://doi.org/10.1038/s41467-025-60206-5.

Correspondence and requests for materials should be addressed to Dongyun Chen or Jian-Mei Lu.

Peer review information *Nature Communications* thanks the anonymous reviewer(s) for their contribution to the peer review of this work. A peer review file is available.

Reprints and permissions information is available at http://www.nature.com/reprints

Publisher's note Springer Nature remains neutral with regard to jurisdictional claims in published maps and institutional affiliations.